



**HAL**  
open science

# Functionalized Electrochemical Aptasensor for Sensing of Ochratoxin A in Cereals Supported by in silico Adsorption Studies

Kwanele Kunene, Myalowenkosi Sabela, Suvardhan Kanchi, Mikhael Bechelany, Krishna Bisetty

## ► To cite this version:

Kwanele Kunene, Myalowenkosi Sabela, Suvardhan Kanchi, Mikhael Bechelany, Krishna Bisetty. Functionalized Electrochemical Aptasensor for Sensing of Ochratoxin A in Cereals Supported by in silico Adsorption Studies. *ACS Food Science & Technology*, 2021, 1 (10), pp.1849-1860. 10.1021/acscitech.1c00226 . hal-03858960

**HAL Id: hal-03858960**

**<https://hal.umontpellier.fr/hal-03858960>**

Submitted on 18 Nov 2022

**HAL** is a multi-disciplinary open access archive for the deposit and dissemination of scientific research documents, whether they are published or not. The documents may come from teaching and research institutions in France or abroad, or from public or private research centers.

L'archive ouverte pluridisciplinaire **HAL**, est destinée au dépôt et à la diffusion de documents scientifiques de niveau recherche, publiés ou non, émanant des établissements d'enseignement et de recherche français ou étrangers, des laboratoires publics ou privés.

# 1 Functionalized Electrochemical Aptasensor for Sensing of Ochratoxin A 2 in Cereals Supported by *in silico* Adsorption Studies

3  
4 Kwanele Kunene<sup>a,b</sup>, Myalowenkosi Sabela<sup>a</sup>, Suvardhan Kanchi<sup>a</sup>, Mikhael Bechelany<sup>b\*</sup> and  
5 Krishna Bisetty<sup>a\*</sup>

6 <sup>a</sup>*Department of Chemistry, Durban University of Technology, P.O. Box 1334, Durban 4000,*  
7 *South Africa*

8 <sup>b</sup>*Institut Européen des Membranes, IEM, UMR 5635, Univ Montpellier, ENSCM, CNRS,*  
9 *34730 Montpellier, France*

## 10 Abstract

11 An aptamer to selectively detect ochratoxin A (OTA) in cereals was developed using silver  
12 nanoparticles (AgNPs) in combination with reduced graphene oxide (rGO). As a result of  
13 characterization experiments conducted in this study, AgNPs were confirmed to be  
14 polydisperse. The electro-catalytic activity was achieved by immobilizing OTA - bovine serum  
15 albumin (OTA - BSA) on the rGO/AgNPs substrate. Based on the experimental conditions  
16 optimized for the aptasensor, the linear dynamic range was 0.002 to 0.016 mg/L and the  
17 threshold was  $7 \times 10^{-4}$  mg/L (S/N = 3). At an atomic and molecular level, computational  
18 adsorption studies revealed how the OTA-BSA interacts with the rGO/AgNPs composite  
19 substrates on a spatial scale. Calculations using density functional theory (DFT) revealed that  
20 OTA has an energy gap of -4.5 eV, which implies a strong tendency to operate as an electron  
21 donor. In addition to its excellent reproducibility and good stability, the proposed aptasensor  
22 demonstrated its applicability in the food industry.

23 *Keywords: Ochratoxin A, AgNPs, reduced Graphene Oxide, electrochemical aptasensor*

24 \_\_\_\_\_  
25 \*Corresponding authors: [bisettyk@dut.ac.za](mailto:bisettyk@dut.ac.za) (K. Bisetty),  
26 [mikhael.bechelany@umontpellier.fr](mailto:mikhael.bechelany@umontpellier.fr) (M. Bechelany)

## 27 1. Introduction

28 Ochratoxin A (OTA) is a metabolite produced by *Penicillium* and *Aspergillus* fungi that  
29 structurally consists of a chlorophenolic group containing a dihydroisocoumarin moiety that is  
30 linked to L-phenylalanine by an amide bond (**Figure S1A**).<sup>1, 2</sup> It has a nephrotoxic,  
31 immunotoxic, teratogenic, mutagenic and carcinogenic effect in both animals and humans.<sup>2, 3</sup>  
32 As a common food contaminant, it enters the human body through the ingestion of  
33 inappropriately stored food products, such as alcoholic products, dried fruits, corn, coffee,  
34 spices and cereal products.<sup>4-9</sup> It is generally accepted that OTA is known to possess  
35 carcinogenic effects as stipulated by the International Agency for Research on Cancer  
36 (IARC).<sup>10</sup> For this reason, as part of the established regulations for OTA in foodstuffs, the  
37 European Commission established the maximum OTA levels for various foods such as spices  
38 (15-20  $\mu\text{g kg}^{-1}$ ), cereal products (3  $\mu\text{g kg}^{-1}$ ), dried fruits (10  $\mu\text{g kg}^{-1}$ ), soluble coffee (10  $\mu\text{g kg}^{-1}$ ),  
39 baby foods (0.5  $\mu\text{g kg}^{-1}$ ) and grape juices (2  $\mu\text{g kg}^{-1}$ ).<sup>11-16</sup> Many different analytical  
40 techniques are available for the detection of OTA. They include high performance liquid  
41 chromatography (HPLC)<sup>17</sup> thin layer chromatography (TLC),<sup>18</sup> liquid chromatography-mass  
42 spectroscopy (LC-MS),<sup>19</sup> gas chromatography-mass spectroscopy (GC-MS)<sup>20</sup> and enzyme-  
43 linked immunosorbent assays (ELISA).<sup>21</sup> Each of these generally acceptable methods has a  
44 limitation, such as low sensitivity, low limits of detection and the need for skilled personnel  
45 with expertise to handle high-end instrumentation. Notably they are costly, time-consuming  
46 and unable to meet the modern-day requirements with high selectivity, good precision, rapid  
47 analysis that is cost effective and easy to operate.

48 Aptamers are single-stranded DNA or RNA oligonucleotide fragments that bind to targets such  
49 as proteins, cells, small ions and molecules. These oligonucleotides are attained by an *in vitro*  
50 Darwinian method called single evolution of ligands by exponential enrichment (SELEX).<sup>22</sup>  
51 They have gained widespread recognition as probes for biomolecular detection, due to their  
52 convenient automated synthesis, high selectivity, stability, adaptable target binding and  
53 flexible modification with a variety of functional groups over antibodies.<sup>23, 24</sup> In recent years,  
54 several aptamer-based detection techniques for OTA including fluorescence,<sup>25</sup> colorimetry,<sup>26</sup>  
55 chemiluminescence<sup>27</sup> and electrochemistry<sup>28</sup> have been reported. There is increasing evidence  
56 which proves that the detection of OTA using electrochemical aptasensors is a powerful  
57 technique, due to fast response, high sensitivity, on-site testing platforms, low background  
58 noise, and good reproducibility.<sup>29, 30</sup> In a recent study by Lv and Wang 2020, they focused on

59 the signal amplification technologies applied to OTA electrochemical aptasensors and  
60 highlighted the current limitations and future challenges.<sup>31</sup> However, to design smart sensing  
61 for mycotoxins, it is crucial to synthesise highly efficient working electrode materials. As a  
62 result of their large specific surface areas, fast electron transfer, and high density of active sites,  
63 noble metal nanoparticles attract considerable research interest.<sup>32</sup> Specifically, AgNPs display  
64 an interesting quantum characteristics, large surface area, small particle diameter and it has the  
65 ability to transfer electron fast.<sup>33</sup> Therefore, AgNPs is widely used in the design of  
66 nanocomposites for electrochemical sensors.<sup>1</sup> Currently, numerous nanomaterials, such as  
67 carbon nanotubes (CNTs), noble metal nanoparticles and graphene oxide (GO) has been used  
68 to fabricate electrochemical sensors.<sup>34-36</sup> Previous reports revealed that GO and reduced  
69 graphene oxide (rGO) has been the key to such research, due to their distinctive properties  
70 including large surface area and high electrochemical conductivity.<sup>37, 38</sup> Several groups have  
71 studied the nanocomposite of graphene-metal nanoparticles for electrochemical sensors for  
72 detection of mycotoxins. Srivastava and co-workers have fabricated nickel nanoparticles  
73 (NiNPs) on rGO for the detection of aflatoxin B (AFB<sub>1</sub>).<sup>39</sup> Shukla and co-worker have  
74 synthesized a reduced graphene oxide/tin oxide (rGO/SnO<sub>2</sub>) nanocomposite for the detection  
75 of patulin in apple juice.<sup>40</sup> Jiang and co-workers reported a synthesis of gold nanoparticles and  
76 reduced graphene oxide (AuNPs-rGO) nanocomposite for the detection of OTA in wine  
77 samples.<sup>41</sup> However, the current literature review has not reported an aptamer-BSA  
78 combination fabricated with AgNPs on rGO for the detection of OTA. It was observed that  
79 there are no reports for the biosynthesis of AgNPs using amadumbe (*Colocasia esculenta*), a  
80 staple diet in the African continent, mainly South Africa, Nigeria and Kenya.<sup>42</sup> Thus, in this  
81 study, a bioinspired AgNP-based probe able to detect OTA using Amadumbe extract will be  
82 developed that is highly sensitive, cost-effective, and eco-friendly.

83 In the current study, a nanocomposite comprising of rGO/AgNPs as an electrochemical sensing  
84 material was used in conjunction with an aptamer-BSA complex for the design of a rapid and  
85 efficient OTA aptasensor. The signal amplification approach was achieved by anchoring the  
86 aptamer onto the surface of rGO/AgNPs and making use of the interaction effect of rGO and  
87 AgNPs fabricated onto carbon screen printed electrodes (C-SPEs). The C-  
88 SPE/rGO/AgNPs/Apt/BSA exhibited good electrocatalytic detection for OTA in food samples.

89 Motivated by the previous work done prompted a combined quantum mechanical and Monte  
90 Carlo simulations implemented to support the experimental methodology. Accordingly, the

91 electronic properties of the OTA in gas phase were investigated, using *ab initio* calculations  
92 based on density functional theory (DFT). An analysis of the adsorption phenomena of these  
93 electrode modifications has been carried out based on Monte Carlo simulations, which have  
94 helped to improve our understanding of important surface phenomena that cannot be  
95 determined just by experimentation.

96 To the best of our knowledge, the computational methodologies were performed in this study  
97 for the first time to assess the electronic and structural properties between the OTA and the  
98 BSA/Aptamer-nanocomposite. New insights into the interactions of OTA with the  
99 nanocomposite can help as a general regulatory guideline for sensing applications in the food  
100 industry.

101

## 102 **2. Experimental section**

### 103 **2.1 Chemicals and reagents**

104 The aptamer sequence 5'-GATCGGGTGTGGGTGGCGTAAAGGGAGCATCGGACA-3',  
105 5'-thionine<sup>43</sup> was purchased from WhiteSci, Whitehead Scientific (Pty) Ltd (Durban, SA).  
106 Amadumbe (*Colocasia esculenta*) and Weet-Bix purchased from a Durban supermarket.  
107 Standards of OTA, (1 mg/mL in dimethyl sulfoxide) and aflatoxin B<sub>1</sub> (AFB<sub>1</sub>), 3.79 µg/g in  
108 acetonitrile were purchased from Sigma-Aldrich, Montpellier, France. Graphite powder, No.1  
109 Whatmann filter paper, silver nitrate (AgNO<sub>3</sub>), bovine serum albumin (BSA), chitosan (CS),  
110 potassium permanganate (KMnO<sub>4</sub>), potassium ferricyanide [Fe(CN)<sub>6</sub>]<sup>3-</sup>, potassium  
111 ferrocyanide [Fe(CN)<sub>6</sub>]<sup>4-</sup>, sodium nitrate (NaNO<sub>3</sub>, monosodium phosphate (NaH<sub>2</sub>PO<sub>4</sub>) and  
112 disodium phosphate (Na<sub>2</sub>HPO<sub>4</sub>) were purchased from Sigma-Aldrich, Durban, SA. Sulphuric  
113 acid (H<sub>2</sub>SO<sub>4</sub>) (97%, v/v), hydrogen peroxide (H<sub>2</sub>O<sub>2</sub>) (30%, w/w), hydrochloric acid (HCl)  
114 (37%, v/v) were purchased from Laboratory Supplies, Durban, SA.

115

### 116 **2.2 Instrumentation**

117 All UV-vis spectrophotometric measurements were performed with VARIAN Cary 50  
118 spectrophotometer (South Africa) in the wavelength ranging 200 to 800 nm. *Colocasia*  
119 *esculenta* extract's functional groups and its role in the formation of nanoparticles were

120 analyzed using an attenuated total reflectance (Cary 630 FTIR Spectrometer from Agilent  
121 Technologies, SA) spectra from 200 to 4000  $\text{cm}^{-1}$ . The particle size analysis of the  
122 biosynthesised AgNPs was performed using Single-particle ICP-MS (PerkinElmer NexION  
123 2000 ICP-MS, Shelton, USA) equipped with the Syngistix nano software. The Asymmetric  
124 Flow Field Flow Fractionation (AF2000) equipped with MALS and UV-vis detectors from  
125 Postnova Analytics, Germany equipped with the AF2000 software was used for the separation  
126 and the hydrodynamic size distribution of the biosynthesized nanoparticles. The morphological  
127 characterization was carried with the high-resolution transmission electron microscopy (HR-  
128 TEM) using a JEOL ARM 200F high-resolution transmission electron microscope (200 kV)  
129 with an EDX analyzer (JED2300, at least 30 accumulations, matrix  $512 \times 512$  points in STEM  
130 mode- X-Max, Oxford Instruments, Germany).

131 The electrochemical measurements were performed at room temperature with a portable  
132 combined bipotentiostat and spectrometer SPELEC Vis-NIR instrument from Metrohm SA.  
133 The three-electrode configuration comprised of a working electrode (WE), a counter electrode  
134 (CE) and a reference electrode (RE). The ProLab oven was used for drying purposes. A 781  
135 pH/Ion meter from Metrohm SA was used for all the pH optimization measurements.

136

### 137 **2.3 Synthesis of Graphene Oxide (GO) and Reduced Graphene Oxide (rGO)**

138 In this work, GO was synthesized from natural graphite by slight modification of the  
139 Hummers' method.<sup>44, 45</sup> Approximately 1.2 g of graphite powder was oxidised by mixing with  
140 2.0 g of  $\text{NaNO}_3$  in 50 mL of concentrated  $\text{H}_2\text{SO}_4$ . The reaction mixture was stirred in an ice  
141 bath for 2 h, at a temperature range of 0-6  $^\circ\text{C}$ , and thereafter 6.0 g of  $\text{KMnO}_4$  was gently added  
142 to the reaction mixture while stirring for another 2 h. Then it was removed from the ice bath  
143 and heated to 30  $^\circ\text{C}$  while stirring for a further 2 h during which the reaction mixture changed  
144 from black into a brownish paste. Then 8% of  $\text{H}_2\text{O}_2$  was added into the reaction to weaken the  
145 paste. At this stage, the colour of the solution changed from brown to golden yellow,  
146 confirming the formation of GO. The resulting mixture was then centrifuged and washed 4  
147 times with 8% HCl and deionized water respectively. Thereafter the filtrate was oven-dried  
148 and crushed into a fine powder. The reduced form of graphene oxide (rGO) was obtained by  
149 using chitosan as a reducing agent in the existing method. The conversion of GO to rGO was  
150 achieved with a 10 x dilution with chitosan (10.0 mg/mL in 1.0% acetic acid) under vigorous

151 stirring for 9 h at 90 °C.<sup>46</sup> The resulting product was then oven-dried at 40 °C for 48 h in order  
152 to obtain a powdered rGO.

153

#### 154 **2.4 Synthesis of Silver Nanoparticles (AgNPs)**

155 The biogenic synthesis of AgNPs was conducted according to a previously reported method.<sup>47</sup>  
156 Fresh samples of amadumbe (*Colocasia esculenta*) as shown in **Figure S1B** were thoroughly  
157 washed with tap water, followed with deionised water, and cut into smaller pieces. To obtain  
158 the aqueous extract, 5.0 g of amadumbe pieces were boiled in 100 mL deionised water at 80  
159 °C for 40 min and allowed to cool at room temperature. After cooling it was filtered through  
160 No.1 Whatmann filter paper. Different parameters such as boiling temperature of the extract,  
161 boiling time and the extracts amount were optimized for the complete reduction of silver. The  
162 filtrate was then used as the reducing agent for the synthesis of AgNPs by adding approximately  
163 4.0 mL of 1.0 mM aqueous AgNO<sub>3</sub>. The mixture was then stirred at 150 rpm for 30 min at 80  
164 °C.

165

#### 166 **2.5 Preparation of rGO/AgNPs nanocomposite**

167 The rGO/AgNPs nanocomposite was prepared by mixing 0.5 mg/mL of rGO and AgNPs in a  
168 ratio of 1:3 (v/v) in 50 mL of deionised water. The mixture was sonicated for 48 h to obtain a  
169 homogenized paste.

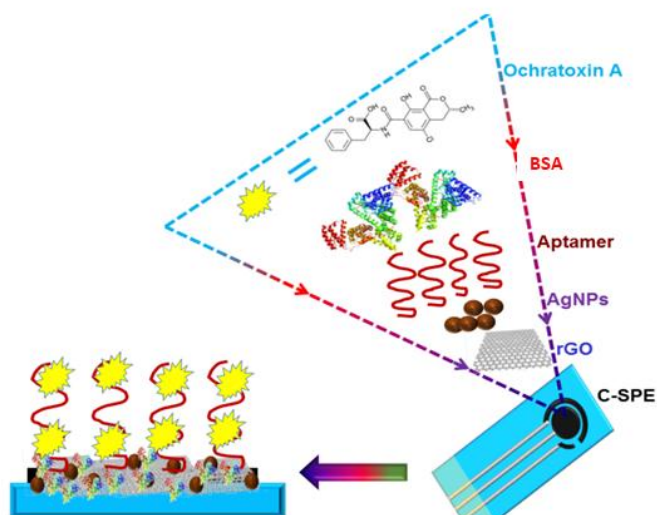
170

#### 171 **2.6 Fabrication of C-SPE/rGO/AgNPs/Apt/BSA aptasensor**

172 The C-SPEs were first activated by applying a constant current of 3 μA for 2 min in 0.1 M  
173 H<sub>2</sub>SO<sub>4</sub> solution rinsed thoroughly with MilliQ-water, and 0.1 M phosphate buffer at pH 7.0.<sup>48</sup>  
174 The activated C-SPE was coated by casting 10.0 μL of rGO/AgNPs paste and dried at 37 °C  
175 for 1 h. Thereafter 10.0 μL of 3.0 μM aptamer was dropped casted onto the rGO/AgNPs and  
176 dried at 24 °C, followed by washing with phosphate buffer to remove the excess (unabsorbed)  
177 aptamer from the C-SPE/rGO/AgNPs/Apt surface. Finally, the electrode was incubated with  
178 1% (v/v) BSA solution for 20 min to completely block the unbound sites of the C-

179 SPE/rGO/AgNPs/Apt surface. The resultant OTA aptasensor electrode comprised of C-  
180 SPE/rGO/AgNPs/Apt/BSA (**Scheme 1**).

181



182

183 **Scheme 1.** Design of the electrochemical OTA aptasensor C-SPE/rGO/AgNPs/Apt/BSA.

184

## 185 **2.7 Sample preparation**

186 The non-contaminated Weet-Bix sample was prepared by following the procedure reported by  
187 He and co-workers.<sup>49</sup> An accurately weighed 4.0 g of the finely grounded sample was mixed  
188 with 10 mL methanol-PBS (60:40, v/v) and allowed to stand for 5 min under ambient  
189 conditions. The mixture was separated by filtration and the resulting methanol filtrate was  
190 spiked with different concentrations of OTA.

191

## 192 **2.8 Characterization techniques**

### 193 **2.8.1 AF4-MALS**

194 The biosynthesised nanoparticles were separated and characterized with an AF4-based system.  
195 The AF4 fractionation conditions are summarized in **Table S1**. AF4-MALS calibration was  
196 performed using polystyrene nanoparticle standard mixtures as described in a previous study.<sup>50</sup>

197



## 198 **2.8.2 SpICP-MS**

199 Single particle ICP-MS analyses were performed, operating in Standard mode as described in  
200 a previous study.<sup>51-54</sup>

201

## 202 **2.8.3 TEM**

203 Morphology studies were undertaken by transmission electron microscopy (TEM) as described  
204 in a previous study.<sup>50</sup>

205

## 206 **2.9 Electrochemical measurements**

207 The CV and DPV measurements were carried out in a redox probe of 1 mM  $[\text{Fe}(\text{CN})_6]^{3-/4-}$   
208 containing 0.1 M PBS. All the electrochemical measurements were performed at room  
209 temperature in the potential range from -0.5 to 0.5 V.

210

## 211 **3. Computational methodology**

### 212 **3.1 Density Functional theory (DFT) Calculations**

213 Gaussian 09<sup>55</sup> was used to perform density functional theory (DFT) calculations on the  
214 geometrically optimized 3D structure of OTA (**Figure S1A**) using the 6-311+G basis sets.  
215 Further confirmation of the global minimum of the optimized geometry was obtained by  
216 calculating the frequency. An important parameter for defining chemical activity is the energy  
217 difference between the highest occupied molecular orbital (HOMO) and the lowest  
218 unoccupied molecular orbital (LUMO), with a smaller value denoting a stronger tendency to  
219 donate electrons. To confirm that the molecule has the ability to accept electrons in the  
220 LUMO, HOMO and LUMO plots have been computed.

221

### 222 **3.2 Construction of the nanomaterials**

223 A 3D model of the GO surface was constructed based on the MS software's standard structural  
224 database and features pristine graphite structures. Graphene oxide (GO) and silver

225 nanoparticles (AgNPs) are modeled using the Material Studio (MS) software package  
226 developed by BIOVIA.<sup>56</sup> For the AgNPs, a 3-D model is defined according to its standard  
227 structural database within MS. In order to assess their feasibility, an energy minimization  
228 procedure was conducted for each, followed by an optimization of geometry using a Forcite  
229 module with an ultrafine-COMPASS force field.<sup>57</sup> In this study, the maximum values of  
230 energy, force, stress, and displacement were set to be  $2 \times 10^{-5}$  kcal/mol, 0.001 kcal/mol, 0.001  
231 GPa, and  $10^{-5}$  Å respectively.

232

### 233 **3.3 Molecular construction of the aptamer sequence**

234 Based on the sequence, the secondary structure of ssDNA was built using M-fold, and refined  
235 equivalent 3D ssRNA models were constructed using Chimera, translated to ssDNA models  
236 by VMD.<sup>58</sup> The BSA (PDB code: 4F5S) structure was extracted from the protein database into  
237 MS to predict the interaction with the aptamer sequences. Discovery Studio visualizer was then  
238 used to explore the aptamer-BSA interaction. The selected aptasensor sequence was then  
239 synthesised by the local supplier.

240

### 241 **3.4 Adsorption Studies by Monte Carlo Simulations**

242 The lowest energy configurations of adsorbates on some selected substrates have been  
243 determined by Monte Carlo (MC) adsorption studies. By replicating the experimental layer-  
244 by-layer electrodes, the substrates and adsorbates were constructed (**Scheme 1**). Adsorption  
245 Locator (AL) functionality (MS software)<sup>56</sup> was used for each generated configuration, thereby  
246 showing the best adsorption sites. Analogues of the electrochemical layer-by-layer strategy  
247 were modelled by carrying out Monte Carlo simulations of the substrate–adsorbate  
248 conformational space since the temperature slowly decreased in accordance with a simulated  
249 annealing strategy during the adsorption process.<sup>56,59</sup>

250 Among the resulting adsorbate-substrate structures, the lowest adsorption energy conformers  
251 were each optimized for a stable conformation, and the adsorption energies are listed in **Table**  
252 **2**.

253

## 254 4. Results and Discussion

### 255 4.1 Experimental section

#### 256 4.1.1 Characterization of biosynthesized AgNPs

##### 257 (i) AF4-MALS

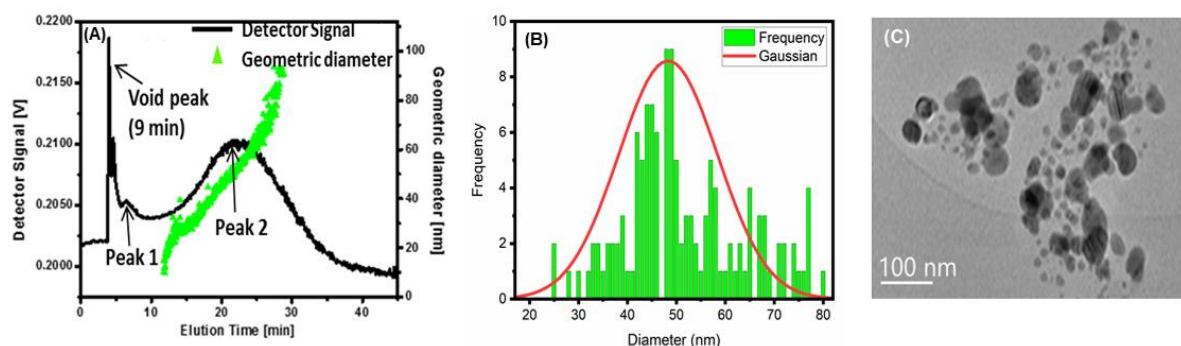
258 The fractogram in **Figure 1A** represents the particle size distribution of AgNPs by AF4-MALS,  
259 under the optimised parameters indicating a clear separation from the void peak. The diameter  
260 of the particles ( $D_{\text{geo}}$ ) for the elution time ranging from 10 to 25 min, results in the average  
261 geometric diameter of 55 nm.

##### 262 (ii) spICP-MS

263 The spICP-MS was used to determine the size of the nanoparticles at low concentrations. The  
264 internal calibration with an isotope dilution was used to determine the size of AgNPs. **Figure**  
265 **1B** revealed a size-based diameter,  $d = 48$  nm.

##### 266 (iii) TEM

267 The size, shape and morphology of AgNPs were identified using transmission electron  
268 microscopy (TEM). The TEM image (**Figure 1C**) confirms that the biosynthesized AgNPs are  
269 spherically shaped, with the average particle size of 53 nm. Veisi and co-workers reported a  
270 spherical shape of AgNPs, when they used plant extract as a reducing agent.<sup>60</sup> The TEM crystal  
271 lattice image (**Figure S1C**) shows the spherical nature of the particles that are highly  
272 crystallized; this is confirmed by the uniform lattice fringes. The lattice spacing of 0.23 nm  
273 corresponds to (111) planes of silver.



274

275 **Figure 1.** (A) AF4-MALS fractogram; (B) spICP-MS and (C) TEM images for biosynthesised AgNPs.

276

#### 277 **4.1.2 Spectroscopic characterization of rGO/AgNPs nanocomposite and C-** 278 **SPE/rGO/AgNPs/Apt/BSA**

##### 279 **(i) UV-Vis spectra**

280 The reduction of Ag (I) to Ag (0) was observed by a colour change from colourless to brown  
281 and it was monitored by UV-Visible (**Figure S1D**). **Figure 2A** shows the UV-Visible spectra  
282 of (i) Amadumbe extract and (ii) AgNPs under the optimized conditions. The surface plasmon  
283 resonance (SPR) absorption band at 428 nm is observed, which is lower than that obtained by  
284 other researchers.<sup>61, 62</sup> This shows that the synthesized AgNPs are spherical in shape, in  
285 agreement with (TEM images in **Figure 1C**) and those reported by Alsharif et al (2020) and  
286 Ndikau et al (2017).<sup>63, 64</sup> The UV-Visible was also used for the characterization of GO and  
287 rGO. A distinct absorption band for GO was observed at 238 nm with a shoulder absorption  
288 band 298 nm (**Figure 2B**). These bands are associated with the  $\pi \rightarrow \pi^*$  aromatic (C=C) and  
289  $n \rightarrow \pi^*$  (C=O) transitions, respectively. Similar results were reported in literature.<sup>65-67</sup> The  
290 absorption band of rGO red shifted to 265 nm depicting an accumulation of electrons and the  
291 removal of some functional groups on the GO surface.<sup>66, 68, 69</sup> The removal of oxygen and the  
292 C=O groups from GO results in the disappearance of the shoulder peak at 298 nm.<sup>69</sup>

293

##### 294 **(ii) ATR spectra**

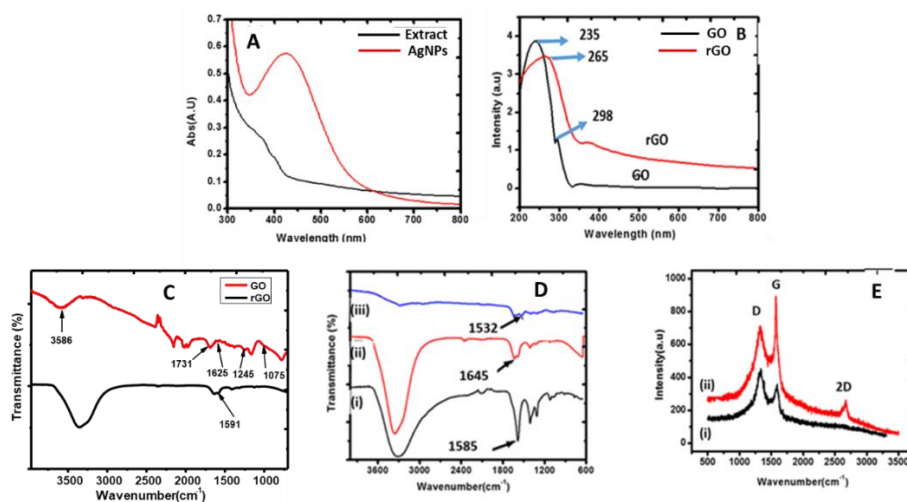
295 The ATR spectroscopy was used to identify the oxygen-containing functional groups that are  
296 present in the synthesised carbonaceous material. The ATR spectrum of GO and rGO (**Figure**  
297 **2C**) shows an intense peak at 3586  $\text{cm}^{-1}$ , corresponding to the O–H groups of the adsorbed  
298 water molecules between the GO sheets, demonstrating the hydrophilic characteristic of GO.  
299 The C=O stretching, aromatic C=C vibrations, epoxy C-O stretching vibration and the alkoxy  
300 C–O stretching vibrations were observed at 1731, 1625, 1245 and 1075  $\text{cm}^{-1}$  respectively in the  
301 GO spectrum.<sup>70-74</sup> After the reduction of the GO, the peak at 1731  $\text{cm}^{-1}$  disappeared, suggesting  
302 the elimination of the oxygen-containing functional groups, such as C=O and C-O bonds.<sup>75, 76</sup>  
303 The intense peak at 1591  $\text{cm}^{-1}$  indicates the restoration of the  $\text{sp}^2$  carbon networks.<sup>77</sup> The  
304 functional groups that are present in all fabrication steps of the aptasensor as shown in **Figure**  
305 **2D**. The ATR spectra of C-SPE rGO/AgNPs shown in **Figure 2D (i)** is similar to that of rGO

306 but there is a weak intensity with a minor blue shift from 1585 to 1591  $\text{cm}^{-1}$ , arising from the  
 307 large presence of AgNPs.<sup>78</sup> After the immobilization of the aptamer onto the electrode surface,  
 308 **Figure 2D (ii)**, the C=O peak at 1645  $\text{cm}^{-1}$  was observed, this confirmed the formation of  
 309 metal-DNA aptamer bonding on the electrode surface.<sup>79</sup> The incubation of the blocking agent,  
 310 BSA, on the electrode surface resulted in the secondary amide peak at 1532  $\text{cm}^{-1}$ , indeed  
 311 confirming the adsorption.

312

### 313 (iii) Raman Spectra

314 The Raman spectroscopy was used to characterize rGO before and after AgNPs were absorbed  
 315 on the surface as shown in **Figure 2E**. The graphite spectrum is characterized by the G and D-  
 316 bands. These two main bands are attributed to the disorder in the C-C bonds and the in-plane  
 317 vibration bonds respectively.<sup>80</sup> The 2 characteristic D and G bands around 1320  $\text{cm}^{-1}$  and 1586  
 318  $\text{cm}^{-1}$  were observed on the rGO spectra before AgNPs modification (**Figure 2E (i)**). The D  
 319 band provides information of the breathing mode of the k-point, while the G band relates to the  
 320 tangential stretching mode of the  $E_{2g}$  phonon of the  $sp^2$  carbon atoms.<sup>81</sup> After the AgNPs were  
 321 decorated onto the rGO, the intensity of D and G bands observed at 1327  $\text{cm}^{-1}$  and 1574  $\text{cm}^{-1}$   
 322 respectively were then enhanced (**Figure 2E (ii)**) because of the surface enhanced Raman  
 323 scattering of nanoparticles.



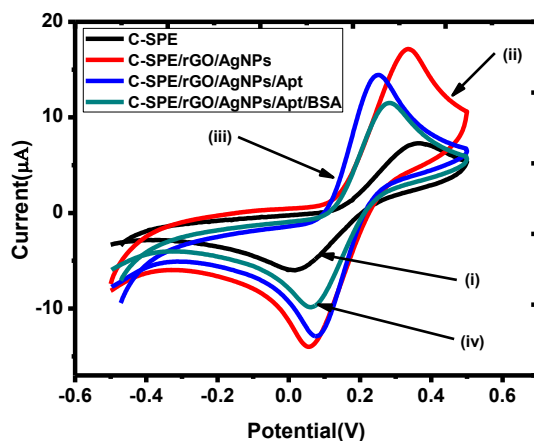
324

325 **Figure 2.** UV-Vis spectra of (A) AgNPs and Amadumbe extract, (B) GO and rGO; ATR spectra of (C) GO and  
 326 rGO; and (D) (i) C-SPE/rGO/AgNPs, (ii) C-SPE/rGO/AgNPs/Apt, and (iii) C-SPE/rGO/AgNPs/Apt/BSA; and  
 327 (E) Raman spectra of (i) rGO and (ii) rGO/AgNPs.

328

### 329 4.1.3 Electrochemical characterization of C-SPE/rGO/AgNPs/Apt/BSA

330 Cyclic voltammetry (CV) is one of the most useful techniques in the evaluation of the  
331 electrochemical behaviour of modified electrodes. **Figure 3** shows the cyclic voltammograms  
332 attained at the fabricated aptasensor in 5.0 mM  $[\text{Fe}(\text{CN})_6]^{3-/4-}$  prepared in a 0.1 M PBS buffer  
333 at pH 7. The bare C-SPEs displayed a well-defined redox peak which corresponds to the  
334 reversible redox reaction of  $[\text{Fe}(\text{CN})_6]^{3-/4-}$ . After deposition of rGO/AgNPs composite, a  
335 significant increase in the redox peak current was observed, due to the presence of improved  
336 conductivity properties of rGO and AgNPs. The rGO/AgNPs composite promoted an electron  
337 transfer because of the increased surface area. The oxygen groups in GO provided a selective  
338 interface for the deposition of AgNPs. The  $\pi$ - $\pi$  stacking interaction present in rGO accelerated  
339 the electron transfer and AgNPs conductivity.<sup>82</sup> After immobilization of the aptamer, a  
340 decrease in the redox peak suggests that the presence of the aptamer on the electrode surface  
341 hinders the electron transfer.<sup>83</sup> A further decrease in the peak current was observed on  
342 immobilization of BSA due to the blocking of the non-specific binding sites of the aptasensor,  
343 demonstrating a successful immobilization onto the electrode surface. The anodic peak  
344 potential ( $E_{\text{pa}}$ ) shifts towards the left, while the cathodic peak potential ( $E_{\text{pc}}$ ) shifts towards the  
345 right, this indicates an efficient mass transfer between the modified electrodes.<sup>84</sup>



346

347 **Figure 3.** Comparative cyclic voltammograms of (i) bare C-SPE, (ii) C-SPE/rGO/AgNPs, (iii) C-  
348 SPE/rGO/AgNPs/Apt and (iv) C-SPE/rGO/AgNPs/Apt/BSA in 1 mM  $[\text{Fe}(\text{CN})_6]^{3-/4-}$  and 0.1 M PBS (pH 7.0) at  
349 a scan rate of 20 mV/s and (B) dependence of the peak potential shift at different electrode types.

350

#### 351 4.1.4 Optimization of experimental conditions

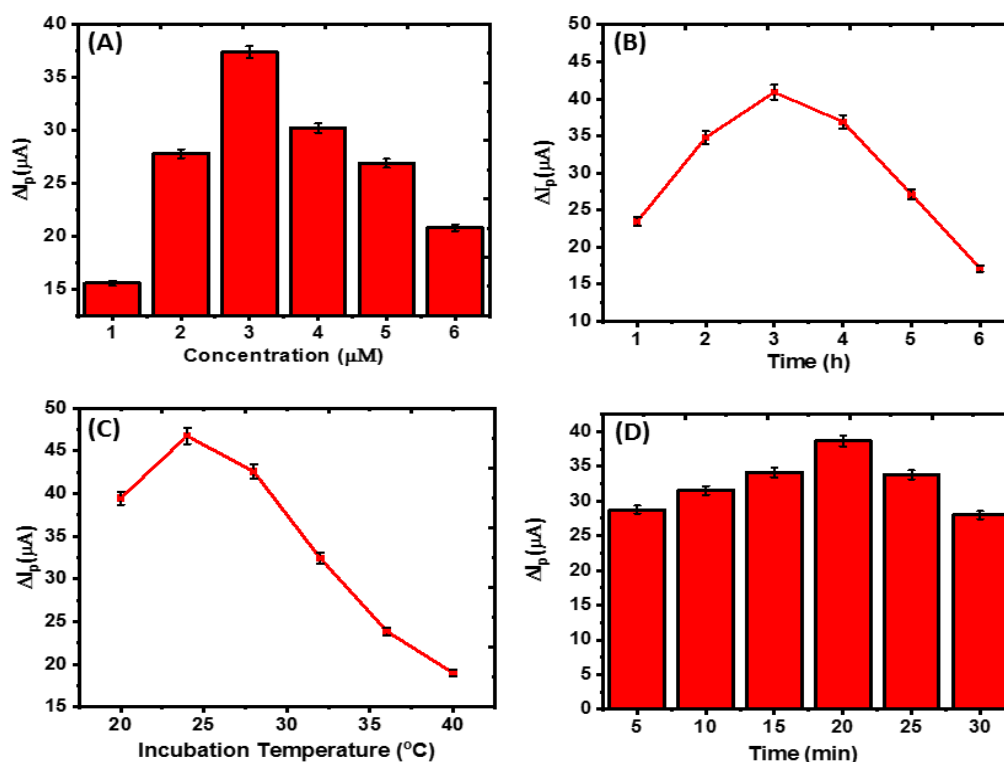
352 In order to attain an outstanding analytical performance of the proposed aptasensor, the ratio,  
353 aptamer concentration, incubation time, incubation temperature, the OTA incubation time, and  
354 pH were optimized. The peak currents gradually increase with increasing rGO: AgNPs ratios  
355 (**Figure S2A**), because of the deposition of more metallic AgNPs with good electroactivity  
356 onto the modified electrode. The optimum value of the peak currents were observed at a ratio  
357 of 1:3, beyond which it decreases due to the reduction of the electron transfer efficiency. This  
358 is a significant result as it also limits the amount of aptamer immobilized onto the C-  
359 SPE/rGO/AgNPs surface.

360 The effect of the aptamer concentration was studied by modifying the electrode with  
361 concentrations ranging from 1 to 6  $\mu\text{M}$  as shown on **Figure 4A**. The current response increases  
362 from 1 to 3  $\mu\text{M}$  with a maximum of 37.5  $\mu\text{A}$ , and thereafter decreases because of a poor  
363 interfacial electron transfer of the aptamer. The incubation time of the 3  $\mu\text{M}$  aptamer was  
364 optimized by monitoring the current responses for 6 h (**Figure 4B**). There is an increase in  
365 current with increasing incubation time reaching a maximum of  $\Delta I_{\text{pa}}$  at 3 h, beyond which it  
366 decreases due to a longer incubation time, resulting in the partial hybridization of the aptamer.  
367 Consequently, 3 h was selected as the optimum incubation time.

368 DNA has a specified working temperature due to the presence of different functional groups  
369 that may affect the incubation temperature when fabricating the aptasensor. **Figure 4C** shows  
370 an increase in  $\Delta I_{\text{pa}}$  results in an increase of the incubation temperature up to 24  $^{\circ}\text{C}$  and thereafter  
371 it gradually decreases. Peng and co-workers revealed that the high incubation temperature  
372 decomposes the aptamer.<sup>85</sup> Therefore 24  $^{\circ}\text{C}$  of the incubation time was used for the entire  
373 experiment. This demonstrates the optimum performance of the DNA at room temperature, in  
374 accordance with the accompanying safety sheet provided by supplier, Whitehead Scientific  
375 (Pty). The analytical performance of the aptasensor on the recognition time of aptamer to OTA  
376 was also evaluated as shown in **Figure 4D**. The current response increased with an increasing  
377 of the incubation time from 5 to 20 min. When the incubation time was more than 20 min, the  
378 current response decreases, suggesting that the bio-recognition reaction was completed. Hence,  
379 20 min of incubation time was chosen. pH value is another significant factor that affects the  
380 response of the sensor. Su and co-workers previously reported that an acidic and basic  
381 environment could damage the negatively-charged aptamer and therefore affects the interaction

382 between the aptamer and their targets.<sup>86</sup> The effect of pH on the current response of the C-  
383 SPE/rGO/AgNPs/Apt/BSA towards OTA was evaluated at pH 4 to 8 (**Figure S2B**). The current  
384 response towards OTA increases until it reaches pH 7 and then it decreases. This result  
385 confirms that the aptasensor performance is pH dependent; hence all the electrochemical  
386 measurements were conducted at pH 7 to ensure that the fabricated aptasensor functions at its  
387 maximum sensitivity.

388



389

390 **Figure 4.** Effect of the aptamer (A) concentration, (B) incubation time, (C) incubation temperature; and (D) Effect  
391 of OTA incubation time.

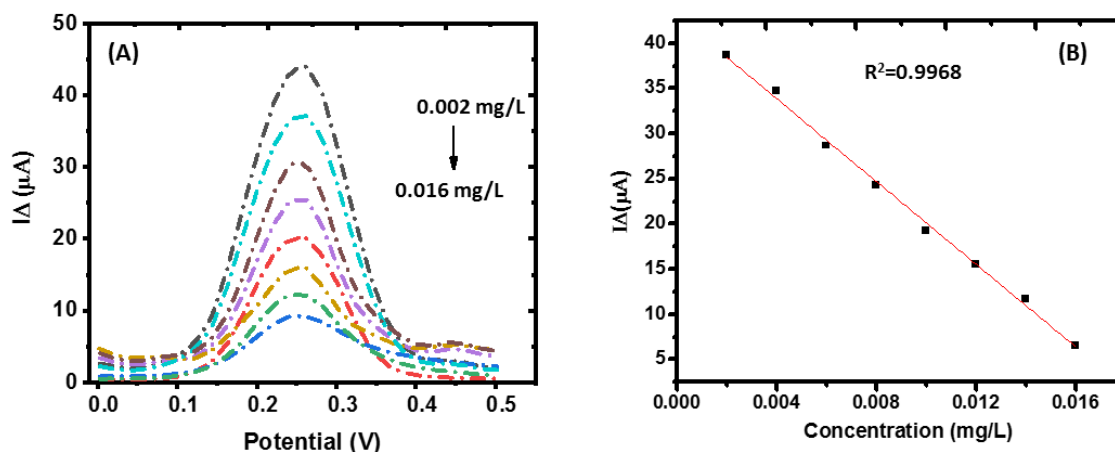
392

#### 393 4.1.5 Analytical performance of the fabricated aptasensor

394 The analytical performance of the fabricated aptasensor was examined by assessing the DPV  
395 current response of the aptasensor incubated with OTA concentrations ranging from 0.002 to  
396 0.016 mg/L. **Figure 5A** shows a linearly decreasing peak current with an increasing OTA  
397 concentration. This shows that the aptamer was folded and the formation of OTA-Apt  
398 complexes on the sensing interface causes inhibition of electron transfer of the redox probe



399  $[\text{Fe}(\text{CN})_6]^{3-/4-}$ . Quantitative detection of OTA was then carried out by observing the decrease  
400 of DPV responses of  $[\text{Fe}(\text{CN})_6]^{3-/4-}$  peak current by increasing OTA concentration. Under the  
401 optimal conditions, the calibration curve of the fabricated aptasensor yielded a linear range  
402 from 0.002 to 0.016 mg/L with a correlation coefficient of 0.9968 (**Figure 5B**). The LOD was  
403  $7 \times 10^{-4}$  mg/L, and with a similar linear dynamic range observed in previous studies (**Table 1**).  
404



405  
406 **Figure 5.** (A) The DPV response of C-SPE/rGO/AgNPs/Apt/BSA in 1 mM  $[\text{Fe}(\text{CN})_6]^{3-/4-}$  after incubation with  
407 different concentrations of OTA from (0.002-0.016 mg/L); and (B) The linear calibration curve of ( $\Delta I_p$ ) with OTA  
408 concentrations.

409

410 **Table 1. Comparison of the various reported biosensors for the detection of OTA**

411

Strategy	Sensing Technique	Linear range	LOD	Stability (days)	Reference
Apt/SWCNHs	Fluorescence	20–50 Nm	17.2 nM	-	87
dsDNA/PG	Fluorescence	1–1×10 <sup>5</sup> ng/mL	1.0 ng/mL	-	88
G-quadruplex-ThT/FRET	FRET	5–700 ng/mL	0.4 ng/mL	-	89
GCE/CdTe/CS/cDNA/BSA/Cy	(ECL-RET)	5×10 <sup>-4</sup> –50 ng/mL	0.2 pg/mL	5	90
5-pDNA	Fluorescent	5–200 ng/mL	1.3 ng/mL	10	91
Th–Au octahedral–dsDNA/SA–GR/GCE	Electrochemical	0.001–5 ng/mL	0.1 pg mL	14	92
BSA/Apt/AgNP s-rGO/C-SPE	Electrochemical	0.002–0.016 mg/L	7 ×10 <sup>-4</sup> mg/L	20	This work

412 Single-walled carbon nanohorns (SWCNHs), aptamer (Apt), double strand (ds) Deoxyribonucleic acid (DNA),  
 413 Pico Green (PG), fluorescence resonance energy transfer (FRET), electrochemiluminescence resonance energy  
 414 transfer (ECL-RET), glassy carbon electrode (GCE), Cadmium telluride (CdTe), chitosan (CS), capture DNA  
 415 (cDNA), cyanine dye (Cy5), probe DNA (pDNA), Bovine serum albumin (BSA), silver nanoparticles (AgNPs),  
 416 reduced graphene oxide (rGO), carbon screen printed electrode (C-SPE)

417

418 **4.1.6 Specificity, reproducibility and stability of designed aptasensor**

419 To evaluate the specificity of the proposed aptasensor in response to OTA in the presence of  
 420 AFB<sub>1</sub>, the fabricated aptasensor was incubated in a mixture of 0.002 mg/L and 0.01 mg/L of  
 421 OTA and AFB<sub>1</sub> respectively. **Figure S3A** shows a major current response when the aptasensor  
 422 was incubated with 0.002 mg/L of OTA and the mixture, while the incubation of 0.01 mg/L  
 423 AFB<sub>1</sub> showed a negligible DPV signal, indicating that the fabricated aptasensor is highly  
 424 specific towards OTA.

425 The reproducibility of the fabricated aptasensor was studied by the incubation of 0.002 mg/L  
426 OTA in six independent aptasensors. The six measurements with a relative standard deviation  
427 (RSD) of 3.5% (**Figure S3B**), demonstrating a good reproducibility of the fabricated  
428 aptasensor.

429 In addition, the stability of the aptasensor was evaluated for 20 days. Measurements were  
430 recorded at 5-day intervals with an initial current response which decreased to 87.8% (**Figure**  
431 **S3C**), signifying an acceptable stability of the developed aptasensor. The aptasensor was stored  
432 in a refrigerator at 4 °C when not in use.

433

#### 434 **4.1.7 Analytical application of aptasensor**

435 The proposed aptasensor was used for the detection of OTA in Weet-Bix samples. Three OTA  
436 standards were added into the extracted samples, with the recoveries ranging from 94.00 to  
437 106.25% (**Table S1**). These results indicate the reliability and the prospective applicability of  
438 the proposed aptasensor in food security monitoring.

439

#### 440 **4.2 Computational Section**

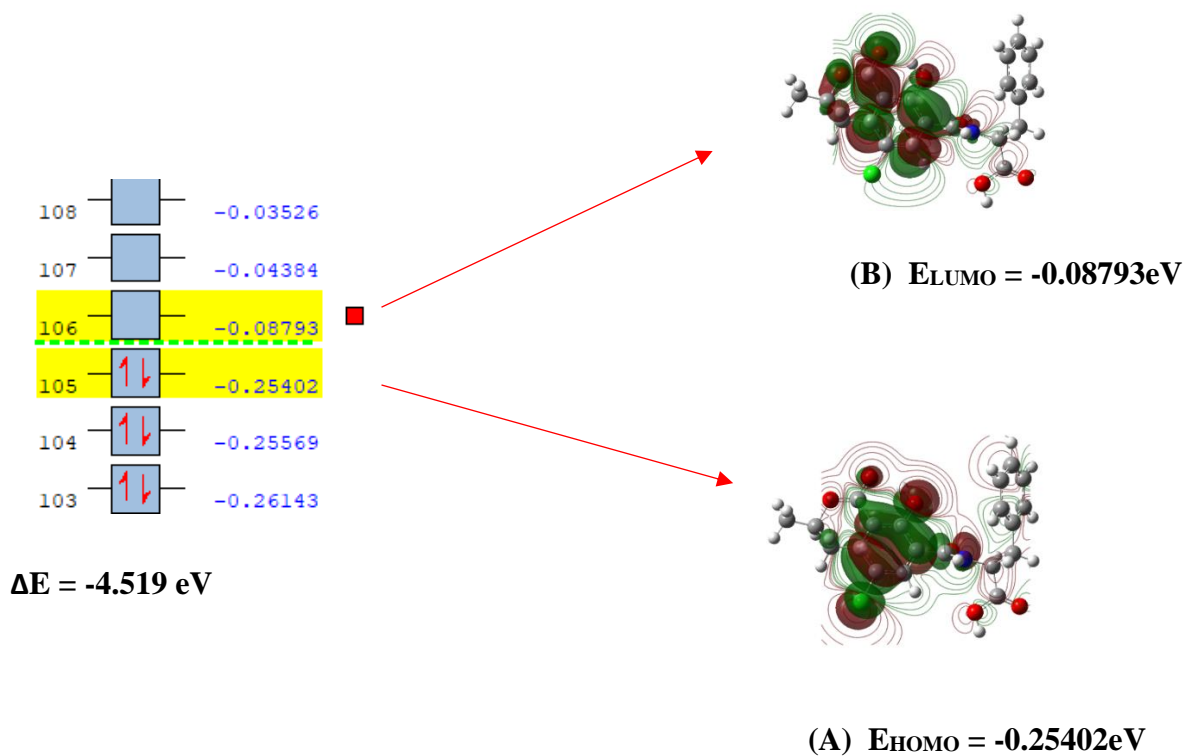
441 In this work, computational modelling was undertaken to better understand the electron transfer  
442 capabilities of OTA, computed at the density functional theory (DFT) level as discussed below.

443

##### 444 **4.2.1 HOMO-LUMO DFT Calculations**

445 **Figure 6A-B** illustrates the HOMO-LUMO plots obtained at the DFT level of theory.  
446 Molecular orbitals with the highest energy are considered to be the highest occupied (HOMO)  
447 and have the ability to donate electrons. This lower unoccupied molecular orbital (LUMO)  
448 informs us that this orbital has an empty electron space, thus suggesting the possibility of  
449 acquiring the donated electrons.<sup>93</sup> The calculated energy gap of -4.519 eV supports this greater  
450 tendency to donate electrons.

451



452 **Figure 6.** The plots for (A) HOMO, (B) LUMO.

453

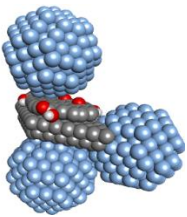
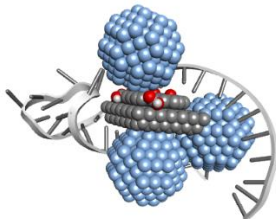

454 In **Figure 6A**, the electrons located in the highest occupied molecular orbitals (HOMO) orbit  
 455 around the oxygen atoms in chlorophenolic groups containing dihydro-isocoumarin rings. In  
 456 accordance with their location, the lowest unoccupied molecular orbitals (LUMO) on  
 457 chlorophenolic rings have dihydro-isocoumarin rings (**Figure 6B**). According to the results  
 458 obtained above, carbonyl groups in esters will be a convenient way for electrons to be added  
 459 to the molecule.

460

#### 461 **4.2.1 Monte Carlo Adsorption Studies**

462 In this section, we used Monte Carlo simulation methods to calculate the adsorption energies  
 463 of amorphous adsorbates and substrates to mimic the experimental electrochemical layers  
 464 (**Scheme 1**). The adsorption energies for the geometry optimized structures are shown in **Table**  
 465 **2** along with an additional energy decomposition based on the adsorption locator algorithm  
 466 (**Table S2**).

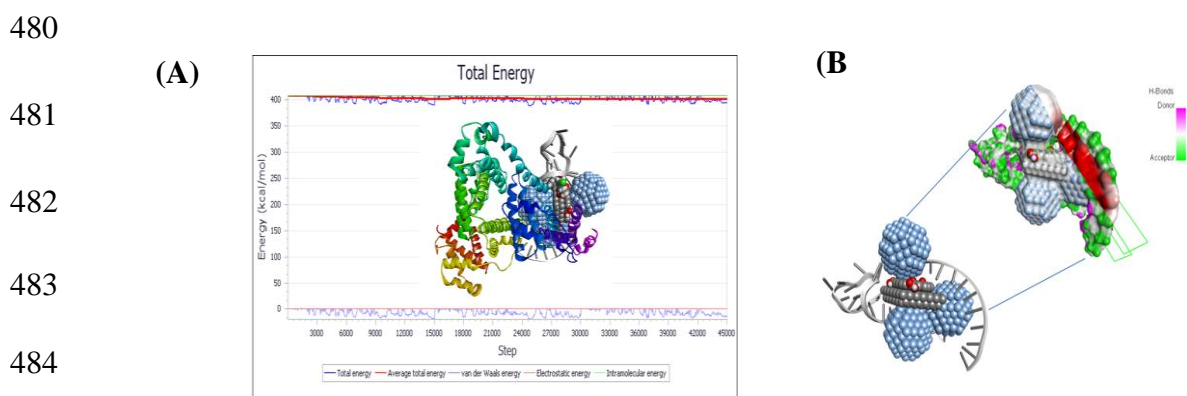
467 **Table 2. The adsorption energy distributions C-SPE/rGO/AgNPs/Apt/BSA**

Substrate	Adsorbate	optimized 3-D structure	adsorption energy kcal/mol
C-SPE/rGO	AgNPs	 <p data-bbox="815 613 1007 640">C-SPE/rGO/AgNPs</p>	<b>-3.1764 x 10<sup>3</sup></b>
C-SPE/rGO/AgNPs	Apt	 <p data-bbox="815 972 1050 999">C-SPE/rGO/AgNPs/Apt</p>	<b>-1.0637 x 10<sup>3</sup></b>
C-SPE/rGO/AgNPs/Apt/	BSA	 <p data-bbox="815 1339 1102 1366">C-SPE/rGO/AgNPs/Apt/BSA</p>	<b>-198.222</b>

468

469

470 Calculated negative adsorption energies indicate stabilization and an exothermic adsorption  
 471 process.<sup>94, 95</sup> The lower the negative energy, the stronger the adsorption between the adsorbate  
 472 and substrate. Based on the increase in the anodic peak current observed at  $E_{pa} = + 0.3V$  in  
 473 **Figure 3** (ii) of our nanocomposite, the presence of the aptamer greatly contributes to its  
 474 stabilization. However, the adsorption energy decreased significantly after BSA was  
 475 immobilized, as confirmed by a reduction in the peak current (**Figure 3** (iv)), due to the  
 476 blocking of the non-specific binding sites of the aptasensor. **Figure 7A** demonstrates the  
 477 presence of an effective bio-molecular interaction between OTA and the aptamer complex, as  
 478 it correlates well with the experimental results. A hydrogen bonded interaction between an  
 479 aptamer and a rGO/AgNPs nanocomposite is shown in **Figure 7B**.



485

486 **Figure 7.** (A) Total energy decomposition plots and 3D representation for SPE/rGO/AgNPs/Apt/BSA-OTA; and  
 487 (B) the corresponding 3D hydrogen bonded interaction plots for SPE/rGO/AgNPs/Apt.

488

## 489 5. Comparison of experimental data with computational results

490 The CV for the layer-by-layer electrode fabrication process (**Figure 3** (ii-iv)) demonstrates a  
 491 linearly decreasing anodic peak current according to the following trend: (ii) C-  
 492 SPE/rGO/AgNPs > (iii) C-SPE/rGO/AgNPs/Apt > (iv) C-SPE/rGO/AgNPs/Apt/BSA. The  
 493 corresponding modelled structures obtained from Monte Carlo simulations resulted in an  
 494 increase in adsorption energy (**Table 2**). This means that the presence of AgNPs fabricated  
 495 onto C-SPE/rGO nanocomposite is most strongly bound and is attributed to the highly negative  
 496 adsorption energy ( $-3.1764 \times 10^3$  kcal/mol) between the adsorbate-substrate system. Our  
 497 simulation results indicate that the highly stabilized (C-SPE/rGO/AgNPs) layer is attributed to

498 the presence of the high energy rGO-AgNPs nanocomposite (**Table S2**), in agreement with the  
499 amplified electrochemical signals depicted in **Figure 3** (ii). On the other hand, the presence of  
500 the aptamer greatly contributes to a lowering of the peak current (**Figure 3** (iii)) with a  
501 corresponding increase in the adsorption energy for the nanocomposite C-  
502 SPE/rGO/AgNPs/Apt. Finally, the adsorption energy increased significantly after the  
503 immobilization of BSA, with a further decrease in the peak current observed in **Figure 3** (iv).  
504 This is attributed to blocking of the non-specific binding sites of the aptasensor as illustrated  
505 in **Figure 7A-B**. Clearly, the highly negative adsorption energy observed when OTA interacted  
506 with the C-SPE/rGO/AgNPs/Apt/BSA, demonstrates the existence of a good bio-molecular  
507 interaction between OTA and the aptamer complex which correlates well with the experimental  
508 results.

509

## 510 **6. Conclusions**

511 The purpose of this study was to develop an electrochemical aptasensor capable of  
512 detecting OTA in commercial Weet-Bix samples with high sensitivity and efficiency. With a  
513 combination of experimental and computational techniques, we demonstrated that the  
514 nanocomposite construction utilizing rGO and AgNP and OTA detector provided good  
515 sensitivity, were easy to use, and were cost effective. Further, all the techniques utilized in this  
516 study allowed simultaneous morphological and size analyses. It can be concluded that AF4-  
517 MALS, spICP-MS, and TEM analyses are accurately inferring the presence of nanoparticles.  
518 According to AF4-MALS analysis, the geometric diameter of AgNPs was 55 nm, while the  
519 mean particle size distribution diameter was 48 nm, and the core size was 53 nm in TEM  
520 analysis. Furthermore, the images obtained by TEM confirmed that the synthesized AgNPs  
521 were spherical in shape. Using the proposed aptasensor, the concentration range was enhanced  
522 from 0.002 to 0.016 mg/L with an LOD of  $7 \times 10^{-4}$  mg/L. Moreover, the presence of AFB<sub>1</sub> did  
523 not show any significant changes in the current. Ample evidence of the effectiveness of the  
524 proposed aptasensor system was obtained when Weet-Bix samples were spiked. A good  
525 recovery was obtained with an acceptable range (94.00 to 106.25%).

526

527 The use of computational modeling has also provided structural information about  
528 interactions between biomolecules and nanostructures, as well as electronic properties of OTA.  
529 Electrochemically modified aptasensors show good agreement with computed adsorption  
530 energies and current responses. Weet-Bix samples can be detected by the proposed aptasensor  
531 using disposable C-SPEs on-site using the disposable C-SPEs.

532

### 533 **Conflict of interest**

534 The authors declare that there is no conflict of interest regarding the publication of this  
535 manuscript.

536

### 537 **Acknowledgements**

538 This work was financially supported by Council for Scientific and Industrial Research  
539 (CSIR), (South Africa). We also acknowledge financial support from the French Embassy  
540 Scholarship from South Africa.

541

### 542 **Supporting Information**

543 Graphical representation of OTA, amadumbe image, HR-TEM image for AgNPs, reduction of  
544 AgNPs, graphical representation of the rGO: AgNPs, representation of pH on change in peak  
545 currents, graphical representation of specificity of the aptasensor in AFB<sub>1</sub>, representation of  
546 reproducibility of the aptasensor with independent electrodes, representation of the storage  
547 stability of the OTA aptasensor, tabulated recoveries of OTA, tabulated energy decomposition.

548

## 549 **7. References**

550 1. Abnous, K.; Danesh, N. M.; Alibolandi, M.; Ramezani, M.; Taghdisi, S. M.,  
551 Amperometric aptasensor for ochratoxin A based on the use of a gold electrode modified with  
552 aptamer, complementary DNA, SWCNTs and the redox marker Methylene Blue.  
553 *Microchimica Acta* **2017**, *184* (4), 1151-1159.



- 554 2. Sánchez-Montero, L.; Córdoba, J. J.; Peromingo, B.; Álvarez, M.; Núñez, F., Effects  
555 of environmental conditions and substrate on growth and ochratoxin A production by  
556 *Penicillium verrucosum* and *Penicillium nordicum*: Relative risk assessment of OTA in dry-  
557 cured meat products. *Food Research International* **2019**, *121*, 604-611.
- 558 3. Paola, B.; Marco, C. L., OTA-grapes: a mechanistic model to predict ochratoxin A risk  
559 in grapes, a step beyond the systems approach. *Toxins* **2015**, *7* (8), 3012-3029.
- 560 4. Jalili, M., Natural occurrence of ochratoxin A contamination in commercial spices in  
561 Tehran. *Nutrition and Food Sciences Research* **2016**, *3* (3), 25-30.
- 562 5. Qi, L.; Li, Y.; Luo, X.; Wang, R.; Zheng, R.; Wang, L.; Li, Y.; Yang, D.; Fang,  
563 W.; Chen, Z., Detoxification of zearalenone and ochratoxin A by ozone and quality evaluation  
564 of ozonised corn. *Food Additives & Contaminants: Part A* **2016**, *33* (11), 1700-1710.
- 565 6. Liu, L.; Xu, L.; Suryoprabowo, S.; Song, S.; Kuang, H., Development of an  
566 immunochromatographic test strip for the detection of ochratoxin A in red wine. *Food and*  
567 *Agricultural Immunology* **2018**, *29* (1), 434-444.
- 568 7. Pei, K.; Xiong, Y.; Li, X.; Jiang, H.; Xiong, Y., Colorimetric ELISA with an acid-  
569 base indicator for sensitive detection of ochratoxin A in corn samples. *Analytical Methods*  
570 **2018**, *10* (1), 30-36.
- 571 8. Chebil, S.; Oueslati, S.; Ben-Amar, A.; Natskoulis, P., Ochratoxigenic fungi and  
572 Ochratoxin A determination in dried grapes marketed in Tunisia. *Annals of Microbiology* **2020**,  
573 *70* (1), 1-9.
- 574 9. Kunene, K.; Weber, M.; Sabela, M.; Voiry, D.; Kanchi, S.; Bisetty, K.; Bechelany,  
575 M., Highly-efficient electrochemical label-free immunosensor for the detection of ochratoxin  
576 A in coffee samples. *Sensors and Actuators B: Chemical* **2020**, *305*, 127438.
- 577 10. Welke, J. E., Fungal and mycotoxin problems in grape juice and wine industries.  
578 *Current Opinion in Food Science* **2019**, *29*, 7-13.
- 579 11. Cappozzo, J.; Jackson, L.; Lee, H. J.; Zhou, W.; Al-Taher, F.; Zweigenbaum, J.;  
580 Ryu, D., Occurrence of ochratoxin A in infant foods in the United States. *Journal of food*  
581 *protection* **2017**, *80* (2), 251-256.
- 582 12. Heshmati, A.; Zohrevand, T.; Khaneghah, A. M.; Nejad, A. S. M.; Sant'Ana, A. S.,  
583 Co-occurrence of aflatoxins and ochratoxin A in dried fruits in Iran: Dietary exposure risk  
584 assessment. *Food and Chemical Toxicology* **2017**, *106*, 202-208.
- 585 13. Jedidi, I.; Cruz, A.; González-Jaén, M. T.; Said, S., Aflatoxins and ochratoxin A and  
586 their *Aspergillus* causal species in Tunisian cereals. *Food Additives & Contaminants: Part B*  
587 **2017**, *10* (1), 51-58.
- 588 14. Sun, Z.; Wang, X.; Tang, Z.; Chen, Q.; Liu, X., Development of a biotin-streptavidin-  
589 amplified nanobody-based ELISA for ochratoxin A in cereal. *Ecotoxicology and*  
590 *environmental safety* **2019**, *171*, 382-388.

- 591 15. Khaneghah, A. M.; Fakhri, Y.; Abdi, L.; Coppa, C. F. S. C.; Franco, L. T.; de Oliveira,  
592 C. A. F., The concentration and prevalence of ochratoxin A in coffee and coffee-based  
593 products: A global systematic review, meta-analysis and meta-regression. *Fungal biology*  
594 **2019**, *123* (8), 611-617.
- 595 16. Leal, T.; Abrunhosa, L.; Domingues, L.; Venâncio, A.; Oliveira, C., BSA-based  
596 sample clean-up columns for ochratoxin A determination in wine: Method development and  
597 validation. *Food chemistry* **2019**, *300*, 125204.
- 598 17. Lhotská, I.; Šatínský, D.; Havlíková, L.; Solich, P., A fully automated and fast method  
599 using direct sample injection combined with fused-core column on-line SPE–HPLC for  
600 determination of ochratoxin A and citrinin in lager beers. *Analytical and bioanalytical*  
601 *chemistry* **2016**, *408* (12), 3319-3329.
- 602 18. Casoni, D.; Badea, M.; Bros, I.; Cobzac, S. C. A., Investigation on image processing  
603 parameters for plate evaluation in TLC analysis of mycotoxins. *Stud. Univ. Babeş Bolyai Chem*  
604 **2017**, *62*, 89-102.
- 605 19. Elaridi, J.; Yamani, O.; Al Matari, A.; Dakroub, S.; Attieh, Z., Determination of  
606 ochratoxin A (OTA), ochratoxin B (OTB), T-2, and HT-2 toxins in wheat grains, wheat flour,  
607 and bread in Lebanon by LC-MS/MS. *Toxins* **2019**, *11* (8), 471.
- 608 20. Zhang, X.; Li, M.; Cheng, Z.; Ma, L.; Zhao, L.; Li, J., A comparison of electronic  
609 nose and gas chromatography–mass spectrometry on discrimination and prediction of  
610 ochratoxin A content in *Aspergillus carbonarius* cultured grape-based medium. *Food chemistry*  
611 **2019**, *297*, 124850.
- 612 21. Fadlalla, M. H.; Ling, S.; Wang, R.; Li, X.; Yuan, J.; Xiao, S.; Wang, K.; Tang, S.;  
613 Elsir, H.; Wang, S., Development of ELISA and Lateral Flow Immunoassays for Ochratoxins  
614 (OTA and OTB) Detection Based on Monoclonal Antibody. *Frontiers in cellular and infection*  
615 *microbiology* **2020**, *10*, 80.
- 616 22. Röthlisberger, P.; Hollenstein, M., Aptamer chemistry. *Advanced drug delivery reviews*  
617 **2018**, *134*, 3-21.
- 618 23. Wang, L.; Ma, W.; Chen, W.; Liu, L.; Ma, W.; Zhu, Y.; Xu, L.; Kuang, H.; Xu, C.,  
619 An aptamer-based chromatographic strip assay for sensitive toxin semi-quantitative detection.  
620 *Biosensors and Bioelectronics* **2011**, *26* (6), 3059-3062.
- 621 24. Hao, N.; Jiang, L.; Qian, J.; Wang, K., Ultrasensitive electrochemical Ochratoxin A  
622 aptasensor based on CdTe quantum dots functionalized graphene/Au nanocomposites and  
623 magnetic separation. *Journal of Electroanalytical Chemistry* **2016**, *781*, 332-338.
- 624 25. He, Y.; Tian, F.; Zhou, J.; Jiao, B., A fluorescent aptasensor for ochratoxin A detection  
625 based on enzymatically generated copper nanoparticles with a polythymine scaffold.  
626 *Microchimica Acta* **2019**, *186* (3), 1-7.
- 627 26. Tian, F.; Zhou, J.; Jiao, B.; He, Y., A nanozyme-based cascade colorimetric aptasensor  
628 for amplified detection of ochratoxin A. *Nanoscale* **2019**, *11* (19), 9547-9555.

- 629 27. Yan, X.-L.; Xue, X.-X.; Luo, J.; Jian, Y.-T.; Tong, L.; Zheng, X.-J., Construction of  
630 chemiluminescence aptasensor platform using magnetic microsphere for ochratoxin A  
631 detection based on G bases derivative reaction and Au NPs catalyzing luminol system. *Sensors*  
632 *and Actuators B: Chemical* **2020**, *320*, 128375.
- 633 28. Taghdisi, S. M.; Danesh, N. M.; Ramezani, M.; Alibolandi, M.; Nameghi, M. A.;  
634 Gerayelou, G.; Abnous, K., A novel electrochemical aptasensor for ochratoxin a sensing in  
635 spiked food using strand-displacement polymerase reaction. *Talanta* **2021**, *223*, 121705.
- 636 29. Liu, S.; Wang, Y.; Xu, W.; Leng, X.; Wang, H.; Guo, Y.; Huang, J., A novel  
637 sandwich-type electrochemical aptasensor based on GR-3D Au and aptamer-AuNPs-HRP for  
638 sensitive detection of oxytetracycline. *Biosensors and Bioelectronics* **2017**, *88*, 181-187.
- 639 30. Zeng, R.; Su, L.; Luo, Z.; Zhang, L.; Lu, M.; Tang, D., Ultrasensitive and label-free  
640 electrochemical aptasensor of kanamycin coupling with hybridization chain reaction and  
641 strand-displacement amplification. *Analytica chimica acta* **2018**, *1038*, 21-28.
- 642 31. Lv, L.; Wang, X., Recent advances in ochratoxin A electrochemical biosensors:  
643 Recognition elements, sensitization technologies, and their applications. *Journal of*  
644 *agricultural and food chemistry* **2020**, *68* (17), 4769-4787.
- 645 32. Sang, S.; Li, D.; Zhang, H.; Sun, Y.; Jian, A.; Zhang, Q.; Zhang, W., Facile synthesis  
646 of AgNPs on reduced graphene oxide for highly sensitive simultaneous detection of heavy  
647 metal ions. *RSC advances* **2017**, *7* (35), 21618-21624.
- 648 33. Wei, L.; Lu, J.; Xu, H.; Patel, A.; Chen, Z.-S.; Chen, G., Silver nanoparticles:  
649 synthesis, properties, and therapeutic applications. *Drug discovery today* **2015**, *20* (5), 595-  
650 601.
- 651 34. Shetti, N. P.; Nayak, D. S.; Reddy, K. R.; Aminabhvi, T. M., Graphene-clay-based  
652 hybrid nanostructures for electrochemical sensors and biosensors. In *Graphene-Based*  
653 *Electrochemical Sensors for Biomolecules*, Elsevier: 2019; pp 235-274.
- 654 35. Zhou, Y.; Fang, Y.; Ramasamy, R. P., Non-covalent functionalization of carbon  
655 nanotubes for electrochemical biosensor development. *Sensors* **2019**, *19* (2), 392.
- 656 36. Pan, M.; Yang, J.; Liu, K.; Yin, Z.; Ma, T.; Liu, S.; Xu, L.; Wang, S., Noble metal  
657 nanostructured materials for chemical and biosensing systems. *Nanomaterials* **2020**, *10* (2),  
658 209.
- 659 37. Xuan, X.; Yoon, H. S.; Park, J. Y., A wearable electrochemical glucose sensor based  
660 on simple and low-cost fabrication supported micro-patterned reduced graphene oxide  
661 nanocomposite electrode on flexible substrate. *Biosensors and Bioelectronics* **2018**, *109*, 75-  
662 82.
- 663 38. Ladrón-de-Guevara, A.; Boscá, A.; Pedrós, J.; Climent-Pascual, E.; De Andrés, A.;  
664 Calle, F.; Martínez, J., Reduced graphene oxide/polyaniline electrochemical supercapacitors  
665 fabricated by laser. *Applied Surface Science* **2019**, *467*, 691-697.

- 666 39. Srivastava, S.; Kumar, V.; Arora, K.; Singh, C.; Ali, M. A.; Puri, N. K.; Malhotra,  
667 B. D., Antibody conjugated metal nanoparticle decorated graphene sheets for a mycotoxin  
668 sensor. *RSC advances* **2016**, 6 (61), 56518-56526.
- 669 40. Shukla, S.; Haldorai, Y.; Khan, I.; Kang, S.-M.; Kwak, C. H.; Gandhi, S.; Bajpai,  
670 V. K.; Huh, Y. S.; Han, Y.-K., Bioreceptor-free, sensitive and rapid electrochemical detection  
671 of patulin fungal toxin, using a reduced graphene oxide@ SnO<sub>2</sub> nanocomposite. *Materials*  
672 *Science and Engineering: C* **2020**, 113, 110916.
- 673 41. Jiang, L.; Qian, J.; Yang, X.; Yan, Y.; Liu, Q.; Wang, K.; Wang, K., Amplified  
674 impedimetric aptasensor based on gold nanoparticles covalently bound graphene sheet for the  
675 picomolar detection of ochratoxin A. *Analytica chimica acta* **2014**, 806, 128-135.
- 676 42. Modi, A. T., Effect of indigenous storage method on performance of taro [*Colocasia*  
677 *esculenta* (L.) Schott] under field conditions in a warm subtropical area. *South African Journal*  
678 *of Plant and Soil* **2007**, 24 (4), 214-219.
- 679 43. Zhang, J.; Xu, X.; Qiang, Y., Ultrasensitive electrochemical aptasensor for ochratoxin  
680 A detection using AgPt bimetallic nanoparticles decorated iron-porphyrinic metal-organic  
681 framework for signal amplification. *Sensors and Actuators B: Chemical* **2020**, 312, 127964.
- 682 44. Guerrero-Contreras, J.; Caballero-Briones, F., Graphene oxide powders with different  
683 oxidation degree, prepared by synthesis variations of the Hummers method. *Materials*  
684 *Chemistry and Physics* **2015**, 153, 209-220.
- 685 45. Zaaba, N.; Foo, K.; Hashim, U.; Tan, S.; Liu, W.-W.; Voon, C., Synthesis of graphene  
686 oxide using modified hummers method: solvent influence. *Procedia engineering* **2017**, 184,  
687 469-477.
- 688 46. Ye, Y.; Ding, S.; Ye, Y.; Xu, H.; Cao, X.; Liu, S.; Sun, H., Enzyme-based sensing  
689 of glucose using a glassy carbon electrode modified with a one-pot synthesized nanocomposite  
690 consisting of chitosan, reduced graphene oxide and gold nanoparticles. *Microchimica Acta*  
691 **2015**, 182 (9), 1783-1789.
- 692 47. Tamileswari, R.; Nisha, M. H.; Jesurani, S.; Kanagesan, S.; Hashim, M.; Catherine,  
693 S.; Alexander, P., Synthesis of silver nanoparticles using the vegetable extract of *Raphanus*  
694 *sativus* (radish) and assessment of their antibacterial activity. *Int. J. Adv. Technol. Eng. Sci*  
695 **2015**, 3, 207-212.
- 696 48. Rivas, L.; Mayorga-Martinez, C. C.; Quesada-González, D.; Zamora-Gálvez, A.; de  
697 la Escosura-Muñiz, A.; Merkoçi, A., Label-free impedimetric aptasensor for ochratoxin-A  
698 detection using iridium oxide nanoparticles. *Analytical chemistry* **2015**, 87 (10), 5167-5172.
- 699 49. He, Q.-H.; Xu, Y.; Wang, D.; Kang, M.; Huang, Z.-B.; Li, Y.-P., Simultaneous  
700 multiresidue determination of mycotoxins in cereal samples by polyvinylidene fluoride  
701 membrane based dot immunoassay. *Food chemistry* **2012**, 134 (1), 507-512.
- 702 50. Naidoo, L.; Kanchi, S.; Drexel, R.; Meier, F.; Bisetty, K., Measurement of TiO<sub>2</sub>  
703 Nanoscale Ingredients in Sunscreens by Multidetector AF4, TEM, and spICP-MS Supported  
704 by Computational Modeling. *ACS Applied Nano Materials* **2021**, 4 (5), 4665-4675.

- 705 51. Kim, S. T.; Kim, H. K.; Han, S. H.; Jung, E. C.; Lee, S., Determination of size  
706 distribution of colloidal TiO<sub>2</sub> nanoparticles using sedimentation field-flow fractionation  
707 combined with single particle mode of inductively coupled plasma-mass spectrometry.  
708 *Microchemical Journal* **2013**, *110*, 636-642.
- 709 52. Laborda, F.; Jiménez-Lamana, J.; Bolea, E.; Castillo, J. R., Critical considerations for  
710 the determination of nanoparticle number concentrations, size and number size distributions by  
711 single particle ICP-MS. *Journal of Analytical Atomic Spectrometry* **2013**, *28* (8), 1220-1232.
- 712 53. Yang, Y.; Long, C.-L.; Yang, Z.-G.; Li, H.-P.; Wang, Q., Characterization and  
713 Determination of Silver Nanoparticle Using Single Particle-Inductively Coupled Plasma-Mass  
714 Spectrometry. *Chinese Journal of Analytical Chemistry* **2014**, *42* (11), 1553-1560.
- 715 54. Bisetty, K.; Kanchi, S.; Hloma, P., Evaluation of the catalytic activity of graphene  
716 oxide and zinc oxide nanoparticles on the electrochemical sensing of T1R2-Rebaudioside A  
717 complex supported by in silico methods. *Pure and Applied Chemistry* **2021**.
- 718 55. Frisch, M.; Trucks, G.; Schlegel, H.; Scuseria, G.; Robb, M.; Cheeseman, J.;  
719 Scalmani, G.; Barone, V.; Petersson, G.; Nakatsuji, H., Gaussian 16 revision a. 03. 2016;  
720 gaussian inc. Wallingford CT **2016**, *2* (4).
- 721 56. Naidoo, L.; Suvadhan, K.; Sabela, M. I.; Bisetty, K., Multivariate optimization of  
722 field-flow fractionation of nanoscale synthetic amorphous silica in processed foods supported  
723 by computational modelling. *New Journal of Chemistry* **2020**, *44* (40), 17542-17551.
- 724 57. Sun, H., COMPASS: an ab initio force-field optimized for condensed-phase  
725 applications overview with details on alkane and benzene compounds. *The Journal of Physical*  
726 *Chemistry B* **1998**, *102* (38), 7338-7364.
- 727 58. Jeddi, I.; Saiz, L., Three-dimensional modeling of single stranded DNA hairpins for  
728 aptamer-based biosensors. *Scientific reports* **2017**, *7* (1), 1-13.
- 729 59. Ulicny, J.; Kozar, T. In *Roadmap for Computer-Aided Modeling of Theranostics and*  
730 *Related Nanosystems*, EPJ Web of Conferences, EDP Sciences: 2018; p 05017.
- 731 60. Veisi, H.; Azizi, S.; Mohammadi, P., Green synthesis of the silver nanoparticles  
732 mediated by *Thymra spicata* extract and its application as a heterogeneous and recyclable  
733 nanocatalyst for catalytic reduction of a variety of dyes in water. *Journal of cleaner production*  
734 **2018**, *170*, 1536-1543.
- 735 61. Ahmed, S.; Ahmad, M.; Swami, B. L.; Ikram, S., A review on plants extract mediated  
736 synthesis of silver nanoparticles for antimicrobial applications: a green expertise. *Journal of*  
737 *advanced research* **2016**, *7* (1), 17-28.
- 738 62. Kathiravan, V.; Ravi, S.; Ashokkumar, S., Synthesis of silver nanoparticles from *Melia*  
739 *dubia* leaf extract and their in vitro anticancer activity. *Spectrochimica Acta Part A: Molecular*  
740 *and Biomolecular Spectroscopy* **2014**, *130*, 116-121.
- 741 63. Ndikau, M.; Noah, N. M.; Andala, D. M.; Masika, E., Green synthesis and  
742 characterization of silver nanoparticles using *Citrullus lanatus* fruit rind extract. *International*  
743 *Journal of Analytical Chemistry* **2017**, *2017*.

- 744 64. Alsharif, S. M.; Salem, S. S.; Abdel-Rahman, M. A.; Fouda, A.; Eid, A. M.; Hassan,  
745 S. E.-D.; Awad, M. A.; Mohamed, A. A., Multifunctional properties of spherical silver  
746 nanoparticles fabricated by different microbial taxa. *Heliyon* **2020**, *6* (5), e03943.
- 747 65. Krishna, R.; Titus, E.; Okhay, O.; Gil, J. C.; Ventura, J.; Ramana, E. V.; Gracio, J.  
748 J., Rapid electrochemical synthesis of hydrogenated graphene oxide using Ni nanoparticles.  
749 *Int. J. Electrochem. Sci* **2014**, *9*, 4054-4069.
- 750 66. Emiru, T. F.; Ayele, D. W., Controlled synthesis, characterization and reduction of  
751 graphene oxide: A convenient method for large scale production. *Egyptian Journal of Basic*  
752 *and Applied Sciences* **2017**, *4* (1), 74-79.
- 753 67. Hidayah, N.; Liu, W.-W.; Lai, C.-W.; Noriman, N.; Khe, C.-S.; Hashim, U.; Lee, H.  
754 C. In *Comparison on graphite, graphene oxide and reduced graphene oxide: Synthesis and*  
755 *characterization*, AIP Conference Proceedings, AIP Publishing LLC: 2017; p 150002.
- 756 68. Roy, I.; Sarkar, G.; Mondal, S.; Rana, D.; Bhattacharyya, A.; Saha, N. R.; Adhikari,  
757 A.; Khastgir, D.; Chattopadhyay, S.; Chattopadhyay, D., Synthesis and characterization of  
758 graphene from waste dry cell battery for electronic applications. *RSC advances* **2016**, *6* (13),  
759 10557-10564.
- 760 69. Gebreegziabher, G.; Asemahegne, A.; Ayele, D.; Dhakshnamoorthy, M.; Kumar, A.,  
761 One-step synthesis and characterization of reduced graphene oxide using chemical exfoliation  
762 method. *Materials Today Chemistry* **2019**, *12*, 233-239.
- 763 70. Xu, C.; Shi, X.; Ji, A.; Shi, L.; Zhou, C.; Cui, Y., Fabrication and characteristics of  
764 reduced graphene oxide produced with different green reductants. *PloS one* **2015**, *10* (12),  
765 e0144842.
- 766 71. Husnah, M.; Fakhri, H. A.; Rohman, F.; Aimon, A. H.; Iskandar, F., A modified  
767 Marcano method for improving electrical properties of reduced graphene oxide (rGO).  
768 *Materials Research Express* **2017**, *4* (6), 064001.
- 769 72. Iskandar, F.; Hikmah, U.; Stavila, E.; Aimon, A. H., Microwave-assisted reduction  
770 method under nitrogen atmosphere for synthesis and electrical conductivity improvement of  
771 reduced graphene oxide (rGO). *RSC advances* **2017**, *7* (83), 52391-52397.
- 772 73. Malas, A.; Bharati, A.; Verkinderen, O.; Goderis, B.; Moldenaers, P.; Cardinaels, R.,  
773 Effect of the GO reduction method on the dielectric properties, electrical conductivity and  
774 crystalline behavior of PEO/rGO nanocomposites. *Polymers* **2017**, *9* (11), 613.
- 775 74. He, D.; Peng, Z.; Gong, W.; Luo, Y.; Zhao, P.; Kong, L., Mechanism of a green  
776 graphene oxide reduction with reusable potassium carbonate. *RSC advances* **2015**, *5* (16),  
777 11966-11972.
- 778 75. Gülercan, D.; Gergin, İ.; Sarac, A. S., Preparation and Electrochemical Performances  
779 of graphene oxide/PEDOT and reduced graphene oxide/PEDOT nanofibers and  
780 nanocomposites. *Fibers and Polymers* **2018**, *19* (10), 2178-2187.
- 781 76. Thangavel, P.; Kannan, R.; Ramachandran, B.; Moorthy, G.; Suguna, L.;  
782 Muthuvijayan, V., Development of reduced graphene oxide (rGO)-isabgol nanocomposite

- 783 dressings for enhanced vascularization and accelerated wound healing in normal and diabetic  
784 rats. *Journal of colloid and interface science* **2018**, *517*, 251-264.
- 785 77. Johra, F. T.; Jung, W.-G., Hydrothermally reduced graphene oxide as a supercapacitor.  
786 *Applied Surface Science* **2015**, *357*, 1911-1914.
- 787 78. Yuan, Y.-G.; Gurunathan, S., Combination of graphene oxide–silver nanoparticle  
788 nanocomposites and cisplatin enhances apoptosis and autophagy in human cervical cancer  
789 cells. *International Journal of Nanomedicine* **2017**, *12*, 6537.
- 790 79. Bagheri, R.; Karimzadeh, F.; Kermanpur, A.; Kharaziha, M., The novel  
791 immobilization of G-quadruplex aptamer on Cu deposited surface using electrochemical  
792 method. *Materials Letters* **2021**, *282*, 128703.
- 793 80. Gurunathan, S.; Hyun Park, J.; Choi, Y.-J.; Woong Han, J.; Kim, J.-H., Synthesis of  
794 graphene oxide-silver nanoparticle nanocomposites: an efficient novel antibacterial agent.  
795 *Current Nanoscience* **2016**, *12* (6), 762-773.
- 796 81. Yang, B.; Liu, Z.; Guo, Z.; Zhang, W.; Wan, M.; Qin, X.; Zhong, H., In situ green  
797 synthesis of silver–graphene oxide nanocomposites by using tryptophan as a reducing and  
798 stabilizing agent and their application in SERS. *Applied surface science* **2014**, *316*, 22-27.
- 799 82. Aydogdu, G.; Pekyardimci, S., An electrochemical sandwich-type aptasensor for  
800 determination of lipocalin-2 based on graphene oxide/ polymer composite and gold  
801 nanoparticles. *Talanta* **2020**, *210* (120666).
- 802 83. Liu, S.; Xing, X.; Yu, J.; Lian, W.; Li, J.; Cui, M.; Huang, J., A novel label-free  
803 electrochemical aptasensor based on graphene–polyaniline composite film for dopamine  
804 determination. *Biosensors and Bioelectronics* **2012**, *36* (1), 186-191.
- 805 84. Bojang, A. A.; Wu, H. S., Characterization of electrode performance in enzymatic  
806 biofuel cells using cyclic voltammetry and electrochemical impedance spectroscopy. *Catalysts*  
807 **2020**, *10* (7), 782.
- 808 85. Peng, H.; Hui, Y.; Ren, R.; Wang, B.; Song, S.; He, Y.; Zhang, F., A sensitive  
809 electrochemical aptasensor based on MB-anchored GO for the rapid detection of *Cronobacter*  
810 *sakazakii*. *Journal of Solid State Electrochemistry* **2019**, *23* (12), 3391-3398.
- 811 86. Su, W.; Kim, S.-E.; Cho, M.; Nam, J.-D.; Choe, W.-S.; Lee, Y., Selective detection  
812 of endotoxin using an impedance aptasensor with electrochemically deposited gold  
813 nanoparticles. *Innate immunity* **2013**, *19* (4), 388-397.
- 814 87. Lv, L.; Cui, C.; Liang, C.; Quan, W.; Wang, S.; Guo, Z., Aptamer-based single-  
815 walled carbon nanohorn sensors for ochratoxin A detection. *Food Control* **2016**, *60*, 296-301.
- 816 88. Lv, Z.; Chen, A.; Liu, J.; Guan, Z.; Zhou, Y.; Xu, S.; Yang, S.; Li, C., A simple and  
817 sensitive approach for ochratoxin A detection using a label-free fluorescent aptasensor. *PloS*  
818 *one* **2014**, *9* (1), e85968.

- 819 89. Zeng, H.; Zhu, Y.; Ma, L.; Xia, X.; Li, Y.; Ren, Y.; Zhao, W.; Yang, H.; Deng, R.,  
820 G-quadruplex specific dye-based ratiometric FRET aptasensor for robust and ultrafast  
821 detection of toxin. *Dyes and Pigments* **2019**, *164*, 35-42.
- 822 90. Gao, J.; Chen, Z.; Mao, L.; Zhang, W.; Wen, W.; Zhang, X.; Wang, S.,  
823 Electrochemiluminescent aptasensor based on resonance energy transfer system between CdTe  
824 quantum dots and cyanine dyes for the sensitive detection of Ochratoxin A. *Talanta* **2019**, *199*,  
825 178-183.
- 826 91. Costantini, F.; Lovecchio, N.; Ruggi, A.; Manetti, C.; Nascetti, A.; Reverberi, M.;  
827 de Cesare, G.; Caputo, D., Fluorescent Label-Free Aptasensor Integrated in a Lab-on-Chip  
828 System for the Detection of Ochratoxin A in Beer and Wheat. *ACS Applied Bio Materials* **2019**,  
829 *2* (12), 5880-5887.
- 830 92. Wei, M.; Yue, S.; Zhang, W.; Li, X., Development of an electrochemical aptasensor  
831 using Au octahedra and graphene for signal amplification. *Analytical Methods* **2020**, *12* (3),  
832 317-323.
- 833 93. Kanchi, S.; Sabela, M.; Singh, P.; Bisetty, K., Multivariate optimization of differential  
834 pulse polarographic–catalytic hydrogen wave technique for the determination of nickel (II) in  
835 real samples. *Arabian Journal of Chemistry* **2017**, *10*, S2260-S2272.
- 836 94. Arya, M.; Niklasson, J.; Mohsenzadeh, A.; Bolton, K., A density functional theory  
837 study of reactions of relevance to catalytic hydrocarbon synthesis and combustion. *Theoretical*  
838 *Chemistry Accounts* **2018**, *137* (11), 1-14.
- 839 95. Putri, A. D.; Murti, B. T.; Kanchi, S.; Sabela, M. I.; Bisetty, K.; Tiwari, A.; Asiri,  
840 A. M., Computational studies on the molecular insights of aptamer induced poly (N-  
841 isopropylacrylamide)-graft-graphene oxide for on/off-switchable whole-cell cancer  
842 diagnostics. *Scientific reports* **2019**, *9* (1), 1-14.
- 843